

Structure-Performance Relationship of $\text{LaFe}_{1-x}\text{Co}_x\text{O}_3$ Electrocatalysts for Oxygen Evolution, Isopropanol Oxidation, and Glycerol Oxidation

Ann Cathrin Brix,^[a] Maik Dreyer,^[b] Adarsh Koul,^[a] Moritz Krebs,^[c] Anna Rabe,^[b] Ulrich Hagemann,^[d] Swapnil Varhade,^[a] Corina Andronesco,^[e] Malte Behrens,^{*,[b, c]} Wolfgang Schuhmann,^{*,[a]} and Dulce M. Morales^{*,[f]}

Mitigating high energy costs related to sustainable H_2 production via water electrolysis is important to make this process commercially viable. Possible approaches are the investigation of low-cost, highly active oxygen evolution reaction (OER) catalysts and the exploration of alternative anode reactions, such as the electrocatalytic isopropanol oxidation reaction (iPOR) or the glycerol oxidation reaction (GOR), offering the possibility of simultaneously lowering the anodic overpotential and generating value-added products. A suitable class of catalysts are non-noble metal-based perovskites with the general formula ABO_3 , featuring rare-earth metal cations at the A- and transition metals at the B-site. We synthesised a series of

$\text{LaFe}_{1-x}\text{Co}_x\text{O}_3$ materials with $x=0-0.70$ by automated co-precipitation at constant pH and subsequent calcination at 800°C . X-ray diffraction studies revealed that the phase purity was preserved in samples with $x\leq 0.3$. The activity towards the OER, iPOR, and GOR was investigated by rotating disk electrode voltammetry, showing a relation between structure and metal composition with the activity trends observed for the three reactions. Additionally, GOR product analysis via high-performance liquid chromatography (HPLC) was conducted after 24 and 48 h electrolysis in a circular flow-through cell setup, pointing out a trade-off between activity and selectivity.

Introduction

To achieve clean, sustainable hydrogen production, innovative technologies that do not rely on the utilisation of fossil fuels are required. A suitable candidate is the water electrolyser where the hydrogen evolution reaction (HER) takes place at the cathode and the oxygen evolution reaction (OER) at the anode.^[1,2] Unfortunately, the latter suffers from sluggish kinetics and even state-of-the-art electrocatalysts require high energy costs. Therefore, the investigation of low-cost, highly active and stable OER catalysts is vital to make this process economically feasible. An alternative approach consists in introducing an anodic reaction, replacing the OER, which may offer the possibility of, either or both, lower overpotentials and the generation of value-added products.^[3] For instance, isopropanol, being the smallest secondary alcohol and due to its particular structure, is anodically oxidised to the corresponding C_3 carbonyls without the formation of CO_2 .^[4] Moreover, the isopropanol oxidation reaction (iPOR) offers favourable properties such as low toxicity, low crossover and higher boiling point than e.g. methanol. Another relevant example of an anodic reaction alternative to the OER is the electrocatalytic glycerol oxidation reaction (GOR). Glycerol, as a major by-product of biodiesel production, offers the opportunity of generating value-added compounds as oxidation products (Scheme S11).^[5,6] For example, lactic acid finds applications in different industries such as food, cosmetics, textiles and dairy as pH regulator, preservative, antibacterial and moisturiser,^[7] while glycolic acid serves as a degreasing agent and is used in skin care products.^[8,9]

[a] A. C. Brix, A. Koul, S. Varhade, Prof. Dr. W. Schuhmann
Analytical Chemistry – Center for Electrochemical Sciences (CES)
Faculty of Chemistry and Biochemistry
Ruhr University Bochum
Universitätsstraße 150, 44780 Bochum, Germany
E-mail: wolfgang.schuhmann@rub.de

[b] M. Dreyer, A. Rabe, Prof. Dr. M. Behrens
Faculty for Chemistry, Inorganic Chemistry
University of Duisburg-Essen
Universitätsstraße 7, 45141 Essen, Germany

[c] M. Krebs, Prof. Dr. M. Behrens
Institute of Inorganic Chemistry
Christian-Albrechts-Universität Kiel
Max-Eyth-Straße 2, 24118 Kiel, Germany
E-mail: mbehrens@ac.uni-kiel.de

[d] Dr. U. Hagemann
Interdisciplinary Center for Analytics on the Nanoscale (ICAN)
University of Duisburg-Essen
Carl-Benz-Straße 199, 47057 Duisburg, Germany

[e] C. Andronesco
Chemical Technology III, Faculty of Chemistry and CENIDE
Center for Nanointegration University Duisburg Essen
Carl-Benz-Straße 199, 47057 Duisburg, Germany

[f] Dr. D. M. Morales
Nachwuchsgruppe Gestaltung des Sauerstoffentwicklungsmechanismus
Helmholtz-Zentrum Berlin für Materialien und Energie GmbH
Hahn-Meitner-Platz 1, 14109 Berlin, Germany
E-mail: dulce.morales_hernandez@helmholtz-berlin.de

 Supporting information for this article is available on the WWW under <https://doi.org/10.1002/celec.202200092>

 © 2022 The Authors. ChemElectroChem published by Wiley-VCH GmbH. This is an open access article under the terms of the Creative Commons Attribution Non-Commercial NoDerivs License, which permits use and distribution in any medium, provided the original work is properly cited, the use is non-commercial and no modifications or adaptations are made.

For the aforementioned reactions, high-performance electrocatalysts were reported which made use of noble metal-based materials, for example Ir and Ru oxides in case of the OER,^[10–12] and Pt, Pd and Au-based materials for the iPOR^[4,13–20] and the GOR.^[5,21–32] However, in addition to their scarcity and expensiveness, their severe CO poisoning^[33,34] is problematic for alcohol oxidation as for these reactions all intermediates contain CO species.^[5,6] Thereby, catalysts containing little or no noble metals are highly desirable. Materials based on transition metals such as Fe, Co and Ni are not only less prone to poisoning,^[33] but also abundant, inexpensive, as well as comparatively more stable in alkaline electrolytes where higher activities have been found for alcohol oxidation reactions.^[27] Research efforts were focused on this endeavour,^[35–43] however, a limited number of publications is available especially featuring detailed GOR product analysis.^[6,44–50] Thus, it is of high interest to establish structure-performance relationships for these more complex reactions that include activity alongside product selectivity information.

A suitable candidate class of materials for anodic reactions in water electrolysis are perovskites,^[12,51–58] metal oxides with the general formula ABO₃ consisting typically of rare-earth metals on the A-site, and transition metals on the B-site. The latter directly affects their electrocatalytic properties and changes therein may impact the reaction mechanism.^[12] Recently, a series of LaFe_{1-x}Co_xO₃ samples with x = 0–0.30 were synthesised by semi-automated co-precipitation at constant pH and subsequent calcination at 800 °C.^[52] The obtained materials were investigated as catalysts for gas-phase CO oxidation^[52] as well as for the OER,^[59] while similar materials synthesised via a spray-flame method were used as catalysts for electrocatalytic ethanol oxidation.^[60] In all three cases, these materials showed a strong activation of LaFeO₃ upon incorporation of cobalt in small amounts. Here, we used the coprecipitation approach to fabricate LaFe_{1-x}Co_xO₃ samples with x = 0–0.70, mainly crystallising in the orthorhombic perovskite structure with contributions of rhombohedral perovskite and spinel oxide at high cobalt content.^[61] We investigated the relation between the electrocatalytic activity of the resulting materials for the three different reactions, namely, the OER, iPOR and GOR, and their structure and metal composition. Furthermore, we conducted detailed GOR product analysis to observe the relation between structural characteristics in terms of cobalt content and oxide phase with respect to their potential to convert glycerol to value-added products.

Results and Discussion

LaFe_{1-x}Co_xO₃ samples with nominal x = 0–0.70, which corresponds to the Co/(Co + Fe) fraction, were synthesised via co-precipitation followed by thermal decomposition according to a procedure reported previously.^[52] Surface metal content and surface area of the obtained samples were determined by X-ray photo-electron spectroscopy (XPS) and by the Brunauer-Emmett-Teller (BET) method, respectively. The obtained results are summarised in Table 1. The Co/(Co + Fe) fractions determined from XPS measurements were close to the nominal compositions for all the prepared samples. In the following, we refer to the experimentally determined x-values. The BET surface area ranged between 8 and 25 m² g⁻¹ and showed no systematic trend with Co content. Comparably lower surface areas were obtained for LaFe_{1-x}Co_xO₃ materials with x ≥ 0.50 while the highest values were recorded for x = 0.28 followed by x = 0.11. The double layer capacitance, which is related to the electrochemically active surface area (ECSA) of the sample series, was determined from cyclic voltammograms at various scan rates, followed by an allometric fit of the charging current vs scan rate plot,^[62] showing only a small variation between 9 and 13 μF for the different Co-containing samples.

The impact of replacing Fe with Co in LaFeO₃ on the crystal structure and phase composition was investigated by means of X-ray diffraction (XRD; Figure 1a) showing sharp reflections and, therefore, a high degree of crystallinity. Reflections attributed to LaFeO₃ are shifted to higher angles with increasing Co/(Co + Fe) fraction as the low-spin Co³⁺ ions have a smaller effective ionic radius.^[52] Additional reflections assigned to Co-containing phases become visible for samples exceeding x = 0.50 with an increase in intensity at larger Co/(Co + Fe) fractions. Three different phases were observed in the different samples, namely orthorhombic perovskite, rhombohedral perovskite and cubic spinel (cf. Figure 1b). Samples with x ≤ 0.28 exclusively consisted of the orthorhombic perovskite phase. Materials with larger Co/(Co + Fe) fractions additionally included rhombohedral perovskite and spinel oxides whose contents increased with increasing Co/(Co + Fe) fraction. A shift from orthorhombic to rhombohedral perovskites with increasing Co content is a common phenomenon.^[63,64] The smallest fraction of the total phase composition was made up of the spinel phase,^[61] which might derive from phase segregation in the precursor state where a layered double hydroxide is formed in the otherwise amorphous precursor at higher Co contents, presumably

Table 1. BET surface area and average double layer capacitance of LaFe_{1-x}Co_xO₃ samples.^[a]

x(Co/(Co + Fe)) nominal	x(Co/(Co + Fe)) determined by XPS	Surface area (BET)/m ² g ⁻¹	Average double-layer capacitance (C _{DL})/μF
0	0	16	49.0
0.10	0.11	24	8.4
0.20	0.21	18	12.1
0.30	0.28	25	9.1
0.40	0.36	17	9.6
0.50	0.50	8	13.0
0.60	0.58	9	11.7
0.70	0.69	9	13.3

[a] The values for materials with x = 0–0.30 had been reported previously.^[52,59]

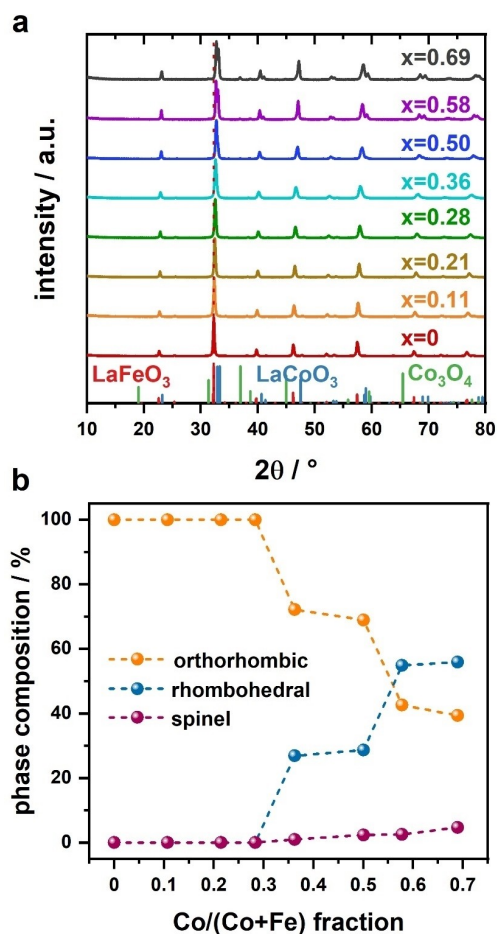


Figure 1. a) X-ray diffractograms of LaFe_{1-x}Co_xO₃ samples and b) their corresponding phase composition determined by Rietveld refinement as a function of the Co/(Co + Fe) fraction *x*. X-ray diffractograms and phase compositions for materials with values for *x* = 0, *x* = 0.11, *x* = 0.21, and *x* = 0.28 were previously reported.^[52,59]

consisting mainly of Fe and Co which means the two elements segregate from La.^[61] Thus, a too high degree of segregation in the precursor state causes the formation of the spinel phase in the calcined materials. Rietveld refinement was conducted for which fit criteria (Table S11) and patterns (Figure S11) as well as a table with the exact percentages of the respective phases (Table S12) are featured in the Supporting Information. Furthermore, it supported the fact that a solid solution was formed in the cationic sublattice as, with increasing *x*-value, a decrease in lattice parameters was observed (cf. Figure S12).

The electrocatalytic activity of the obtained materials towards the OER, iPOR and GOR was investigated by means of rotating disk electrode (RDE) voltammetry in 1 M KOH in the absence or presence of 1 M of the respective alcohol. Measurements were conducted in triplicate to ensure the reliability and reproducibility of the data (cf. Figure S13). The resulting voltammograms are displayed in Figure 2a, 2b and 2c, respectively. Therein, different activity trends can be observed for the OER, iPOR and GOR. For the OER, all Co-containing materials clearly outperformed the Co-free LaFeO₃ sample (cf. Figure 2a). To facilitate the comparison, the potentials corre-

sponding to a current density of 3 mAcm⁻² (*E*_{OER}) were extracted from the voltammograms shown in Figure 2a, and plotted as a function of the Co/(Co+Fe) fraction in Figure 2d (purple). Lower *E*_{OER} values are desirable, since they represent lower overpotentials translating into lower energy costs. The strong decrease in overpotential with respect to the Co-free sample was observed upon incorporation of a small amount of Co, in agreement with previous observations for the same type of materials, which has been attributed to a Co-induced decrease of the binding energy difference of the *O and *OH intermediates during the OER.^[59] Using DFT+U calculations it was found for LaFe_{1-x}Co_xO₃ samples with nominal *x* = 0, 0.125, 0.250, 0.500 that Co incorporation leads to reduced OER overpotential, with a more significant enhancement observed for Co compared to Fe reaction sites. Additionally, incorporating Co led to a variation in magnetic moments at Co reaction sites during OER as well as to a larger fraction of Fe³⁺, especially in deeper layers. Furthermore, a decrease of lattice parameters was observed as B–O–B (i.e. Fe–O–Fe and Co–O–Fe) bond angles deviated from 180° indicating octahedral tilts and rotations which supposedly influence M–O binding strength. The lowest energy configuration was determined to feature low-spin Co³⁺ with high-spin Fe³⁺ as nearest neighbours which, in turn, have Fe neighbours with opposite spin.^[59] In another account in literature, Duan and co-workers^[65] investigated the effect of Fe substitution in LaCoO₃. They found that Co-rich rhombohedral perovskite with 10 at% Fe substitution has superior OER activity compared with mixed and Fe-rich orthorhombic LaFeO₃. They also observed lattice distortion induced by the coexistence of Co and Fe via B–O and O–B–O vibrations probed with FTIR and increasing Fe K pre-edge peak intensity with increasing Fe content in X-ray absorption measurements indicating a decrease in centro-symmetry. A similar coordination environment of Co and Fe atoms was ascertained as well as no significant difference between Co–O and Fe–O bond length alongside Co and Fe valences of approximately 3+. A higher (albeit not too high) Co³⁺ spin state was found to be favourable towards OER coinciding with an insulator-half metal transition due to strong hybridisation of Co (*e_g*) and O (*p*) states. The *E*_{OER} values observed for the phase-pure perovskites with 0.11 ≤ *x* ≤ 0.28 increased nearly linearly with larger Co/(Co + Fe) fractions which may be related to Fe having a beneficial effect on conductivity in mixed metal oxide catalysts.^[66–68] With the change in phase composition, a different OER activity trend was observed, firstly with an increase in *E*_{OER} for LaFe_{0.64}Co_{0.36}O₃, and later with a decrease in the overpotential as the Co/(Co + Fe) ratio increases. This observation indicates that not only the Co/(Co + Fe) fraction but also the phase composition strongly influences the activity of the samples towards the OER. LaFe_{0.31}Co_{0.69}O₃ exhibited the highest OER activity, indicating that both its phase composition and a larger content of Co favour the OER.

For the iPOR (cf. Figure 2b), the observed activity trend in terms of *E*_{iPOR}, namely the potential required to reach 3 mAcm⁻² (cf. Figure 2d, green), was similar to that of the OER. However, the material with the highest iPOR activity was LaFe_{0.89}Co_{0.11}O₃, and, furthermore, the samples with *x* ≤ 0.28 (including the Co-

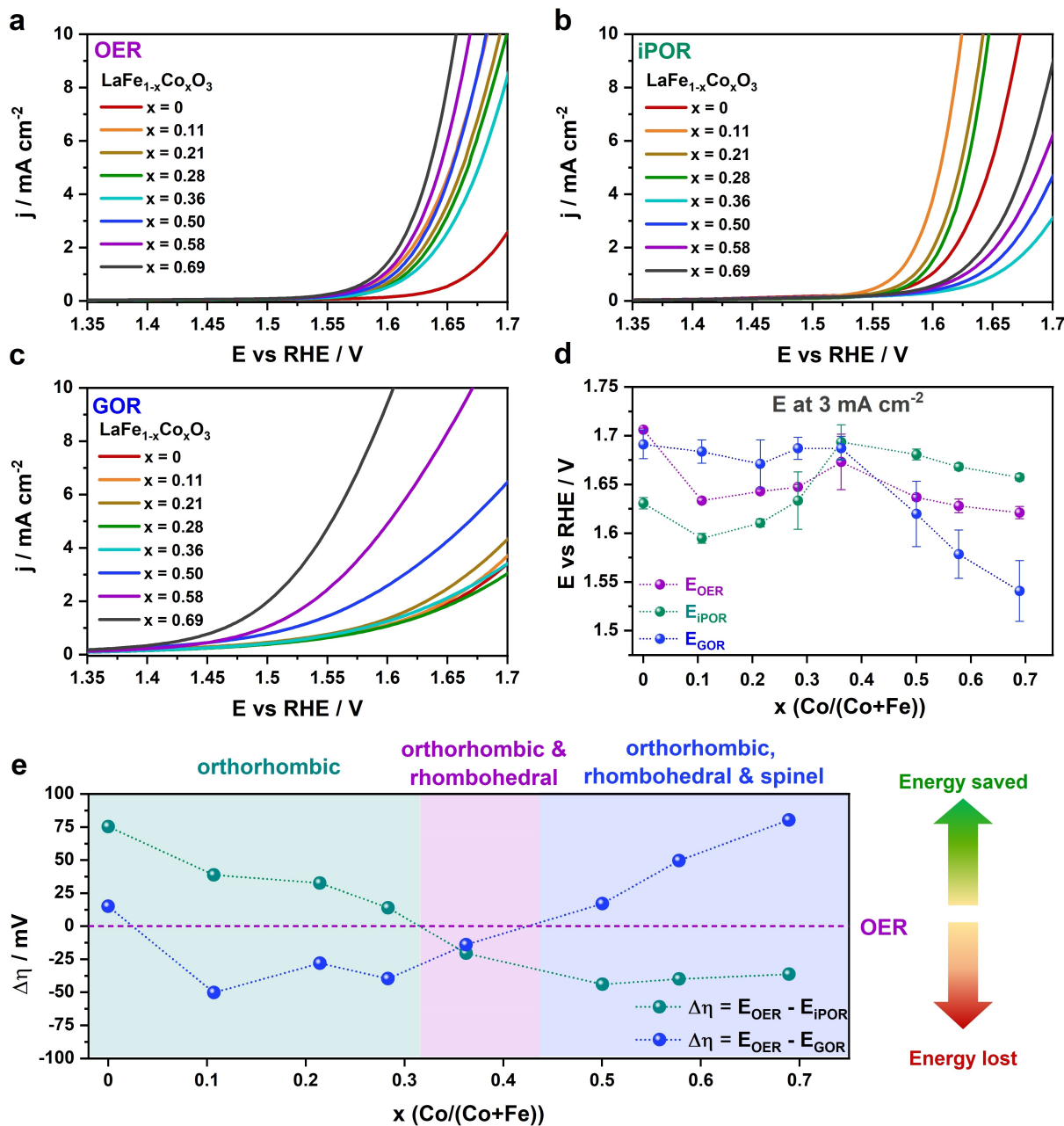


Figure 2. Linear sweep voltammograms of $\text{LaFe}_{1-x}\text{Co}_x\text{O}_3$ materials for a) OER, b) iPOR, and c) GOR, recorded at 5 mV s^{-1} scan rate and 1600 rpm electrode rotation in Ar-saturated KOH (1 M) solutions in the presence or absence of the corresponding alcohol (1 M). d) Comparison of potentials corresponding to the OER, iPOR, and GOR recorded at 3 mA cm^{-2} as a function of the $\text{Co}/(\text{Co} + \text{Fe})$ fraction x . Error bars represent the standard deviation determined from three independent measurements. Dashed lines are included to guide the eye. e) Amount of energy saved ($\Delta\eta$ positive) or lost ($\Delta\eta$ negative) upon replacing the OER with the corresponding alcohol oxidation reaction as anodic process in water electrolysis. $\Delta\eta$ represents the difference in overpotential between the iPOR and the OER (green), and between the GOR and OER (blue), measured at 3 mA cm^{-2} with $\text{LaFe}_{1-x}\text{Co}_x\text{O}_3$ samples as a function of the $\text{Co}/(\text{Co} + \text{Fe})$ ratio x .

free material) displayed the lowest overpotentials within the sample series, indicating more favourable kinetics on the phase-pure orthorhombic perovskite. Interestingly, a different activity trend was observed in the case of the GOR (cf. Figure 2c). The trend of potentials measured at 3 mA cm^{-2} , E_{GOR} (cf. Figure 2d, blue), indicates little change in the activity of the phase-pure samples ($x \leq 0.28$), whereas the $\text{LaFe}_{1-x}\text{Co}_x\text{O}_3$ materials with $x = 0.69, 0.58$ and 0.50 show considerably higher activities with a

substantial decrease in E_{GOR} values with increasing $\text{Co}/(\text{Co} + \text{Fe})$ fraction.

It is important to note that the activity metrics E_{OER} , E_{iPOR} and E_{GOR} did not show any systematic trend in relation to the corresponding BET surface area (Figure SI4a) or to double layer capacitances C_{DL} (the latter being proportional to the ECSA, Figure SI4b), which leads us to the assumption that intrinsic activities have been observed. This is supported by the fact that the material for which the highest C_{DL} was recorded, LaFeO_3 ,

does not show the highest activity in the series for any of the reactions investigated here, in fact in case of the OER, it even exhibits significantly higher overpotential.

A potential advantage of oxidising alcohols instead of evolving oxygen as the anodic reaction in water electrolysis is the decrease in overpotential, which translates to a decrease in energy cost for hydrogen production at the cathode. Oxidising isopropanol resulted in a decrease in overpotential relative to the OER only in the case of the phase-pure samples (Figure 2d), whereas for $\text{LaFe}_{1-x}\text{Co}_x\text{O}_3$ samples with $x > 0.36$ larger overpotentials were required in the presence of isopropanol to achieve the same current density as for the OER. Interestingly, this was different in the case of the GOR, for which the largest decrease in overpotential with respect to the OER was observed with $\text{LaFe}_{0.31}\text{Co}_{0.69}\text{O}_3$. This can be better visualised in Figure 2e, which shows the differences in overpotentials of the iPOR or GOR relative to the OER ($\Delta\eta$) defined as the difference between E_{OER} and E_{iPOR} (green), and between E_{OER} and E_{GOR} (blue), as a function of the $\text{Co}/(\text{Co} + \text{Fe})$ ratio x . Positive $\Delta\eta$ values represent the energy saved upon replacing the OER by the corresponding alcohol oxidation reaction, while a negative $\Delta\eta$ can be understood as an increase in the energy cost with respect to the OER. The dashed line at 0 represents the energy cost of the OER as a reference. It becomes apparent that a benefit of alcohol oxidation over OER strongly depends on the electrocatalyst structure and composition. Namely, for the iPOR energy is saved when using $\text{LaFe}_{1-x}\text{Co}_x\text{O}_3$ materials with x between 0 and 0.28 consisting only of orthorhombic perovskite (cf. Figure 1b), while for the GOR, using $\text{LaFe}_{1-x}\text{Co}_x\text{O}_3$ materials with x between 0.50 and 0.69, where a larger fraction of rhombohedral perovskite and presence of cubic spinel Co_3O_4 are observed (cf. Figure 1a), resulted in saving energy.

For $\text{LaFe}_{1-x}\text{Co}_x\text{O}_3$ with $x = 0.36$, the OER is the best choice in terms of energy requirements, as conducting electrolysis in the presence of either isopropanol or glycerol results in larger overpotentials. These observations show clearly that not only the Co content influences the electrocatalytic activity but also the structure of the material. As such, their effects are difficult to deconvolute as we observed the phase change upon increasing the $\text{Co}/(\text{Co} + \text{Fe})$ fraction. In literature it has also been shown that the Fe/Co ratio has a considerable impact on the OER activity.^[59,65] For instance, Duan and co-workers^[65] have found that Co-rich rhombohedral perovskite exhibits superior activity compared with mixed and Fe-rich orthorhombic LaFeO_3 . For orthorhombic $\text{YCo}_{1-x}\text{Fe}_x\text{O}_3$ materials, increasing methanol oxidation activity was observed with increasing Co content.^[69] Similarly, Alkan and co-workers^[60] found that OER and ethanol oxidation activity decreased upon increasing Fe content in $\text{LaCo}_{1-x}\text{Fe}_x\text{O}_3$, most substantially for the sample containing 60 at% Fe. They also describe the contraction of lattice parameters upon increasing Fe/(Fe + Co) ratio, in agreement with our findings, and obtained orthorhombic perovskite phases at Fe contents greater than 50 at% while rhombohedrally distorted cubic phases were identified at lower Fe contents. The differences between the activity trends observed for the iPOR and the GOR may be related to differences in active site requirements for oxidising monohydric and polyhy-

dric alcohols, as they likely involve different transition states and mechanistic pathways.^[70] In addition to this, it is expected that competition between the OER and the oxidation of either isopropanol or glycerol takes place, however, higher overpotentials were observed in the presence of either alcohol than in their absence, indicating not only a competition but also a hindrance of the OER. This can be explained by the differences in binding strength between the alcohols as well as their intermediates and the catalytic sites, which, in those instances, could lead to poisoning of the electrocatalysts by binding too strongly, thus blocking the active sites. In literature, LaCoO_3 demonstrated resistance to poisoning as the GOR does not take place through formation of strongly adsorbed intermediates.^[50] LaFeO_3 , however, exhibits increased poisoning rates with increasing reactant concentration which was previously described for the methanol oxidation reaction.^[71]

It has been established that the activity of $\text{LaFe}_{1-x}\text{Co}_x\text{O}_3$ towards OER, iPOR and GOR depends strongly on both the cobalt content and the phases present in the catalyst. Out of the sample series, $\text{LaFe}_{0.31}\text{Co}_{0.69}\text{O}_3$ exhibited the lowest overpotentials for electrolysis in the presence of glycerol, reaching a current density of 10 mA cm^{-2} at 1.60 V vs. RHE (cf. Figure 2c). Moreover, this sample also displayed the highest decrease in overpotential with respect to the OER in the presence of glycerol. However, investigation of the selectivity during the GOR is of equal relevance to assess the applicability of these anodic processes.^[72] For the investigation of the relation between structural properties of $\text{LaFe}_{1-x}\text{Co}_x\text{O}_3$ and the products formed during electrolysis in the presence of glycerol, catalysts with $x = 0, 0.11, 0.28, \text{ and } 0.36$ were drop-cast on carbon paper electrodes and mounted in a two-compartment circular flow-through cell setup (cf. Figure S15) using 1 M KOH containing 1 M glycerol as electrolyte solution. Chronoamperograms were recorded at 0.55 V vs. $\text{Ag}|\text{AgCl}|\text{KCl}$ (3 M) (which corresponds to approximately 1.55 V vs. RHE) and are displayed in Figure 3a, showing comparatively larger currents for $\text{LaFe}_{0.31}\text{Co}_{0.69}\text{O}_3$ than for the other three samples in agreement with the voltammetric measurements shown in Figure 2c. In the course of the chronoamperometric measurement, samples were taken at $t = 0, 24, \text{ and } 48 \text{ h}$ for analysis via high-performance liquid chromatography (HPLC) to monitor the concentration of glycerol and the electrolysis products.

As shown in Figure 3b, the concentration of glycerol relative to its concentration at the start of the measurement decreased similarly with increasing electrolysis time for the four samples, accounting for a glycerol conversion of 20 to 30% after 48 h electrolysis. Interestingly, even though the conversion of glycerol was similar for the four catalysts, the total concentration of the products differed considerably (cf. Figure 3c). Likely, after undergoing similar initial glycerol oxidation steps, adsorption of intermediates takes place differently for the four catalysts, leading to large differences in the rates of follow-up reactions, and particularly facilitating further conversion in the case of $\text{LaFe}_{0.31}\text{Co}_{0.69}\text{O}_3$. Upon plotting the total products concentration as a function of $\text{Co}/(\text{Co} + \text{Fe})$ fraction (Figure S16) we observed a linear increase in the phase-pure region, i.e. for $\text{LaFe}_{1-x}\text{Co}_x\text{O}_3$ materials with $x \leq 0.28$. At higher x -values, there is

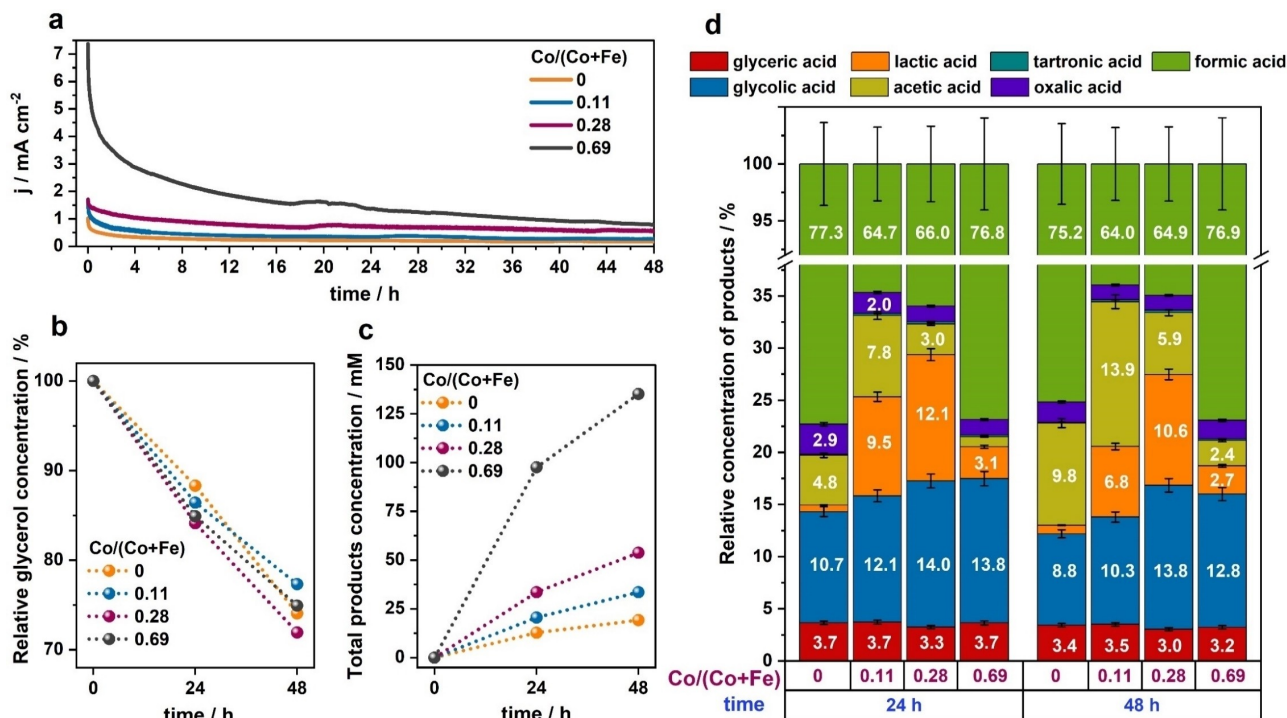


Figure 3. Flow-through cell experiments for glycerol oxidation at $\text{LaFe}_{1-x}\text{Co}_x\text{O}_3$ with $\text{Co}/(\text{Co} + \text{Fe})$ fraction $x = 0, 0.11, 0.28$ and 0.69 . a) Chronoamperometry recorded at $0.55 \text{ V vs. Ag} | \text{AgCl} | \text{KCl} (3 \text{ M})$ in 1 M KOH containing initially 1 M glycerol. b) Concentration of glycerol relative to the initial concentration (1 M), c) total concentration of all products, and d) concentration of electrolysis products relative to the total concentration. The concentrations of glycerol and electrolysis products were determined by HPLC from electrolyte samples collected after $0, 24$, and 48 h electrolysis. Relative concentrations above 2% are indicated in (d) to facilitate comparison.

an even steeper linear increase in product concentration recorded, indicating that in addition to the increase in Co content the presence of a mixture of phases enhances the amount of products detected. Figure 3d shows the composition of electrolyte mixtures, relative to the total concentration of products determined by HPLC, obtained after 24 and 48 h electrolysis time. Chromatograms of standard solutions used for calibration are shown in Figure S17 and the detected product concentrations are listed in Table S13. It is important to note that, while only organic products were detected, it is expected that carbonate is additionally generated. For formic acid, the predominantly formed product for all the four catalysts, the highest relative concentrations were detected for the materials with the lowest and the highest Co content ($\text{Co}/(\text{Co} + \text{Fe})$ ratios $x = 0$ and 0.69 , respectively) for samples collected after 24 h electrolysis. After 48 h , these values are slightly higher, supposedly due to the further oxidation of intermediates which liberate formic acid upon C–C bond cleavage. Yet, $\text{LaFe}_{0.72}\text{Co}_{0.28}\text{O}_3$ yielded the highest relative concentrations of lactic acid and glycolic acid. Interestingly, much higher concentrations of glycolic acid compared to lactic acid were determined for the two catalysts with the highest and the lowest Co contents ($x = 0$ and 0.69), respectively, while the other two materials ($x = 0.28$ and 0.11) showed fairly similar concentrations for the two products (cf. Table S12). The comparison of activity, observed by RDE voltammetry, and the information regarding formation of products determined by HPLC is highly

interesting. $\text{LaFe}_{0.31}\text{Co}_{0.69}\text{O}_3$ displayed the highest GOR activity, the largest amount of energy saved compared to the OER, as well as the highest amount of detected products which makes this sample the most attractive catalyst among the investigated materials. Yet, its selectivity was not the most favourable in terms of valorisation of glycerol. On the one hand, the highest relative formic acid concentration was detected for LaFeO_3 (after 24 h electrolysis). On the other hand, the fraction of more valuable products, considering all products but formate, was highest ($\sim 36\%$) for $\text{LaFe}_{0.89}\text{Co}_{0.11}\text{O}_3$ (after 48 h electrolysis). This clearly shows that there is a trade-off in performance evaluation between activity and selectivity, and that both aspects can be strongly influenced by both the metal and phase composition in the investigated sample series.

Conclusions

A series of $\text{LaFe}_{1-x}\text{Co}_x\text{O}_3$ oxides were synthesised via a coprecipitation method to investigate the impact of the $\text{Co}/(\text{Co} + \text{Fe})$ ratio x on their electrocatalytic properties towards different anodic reactions for water electrolysis, namely the OER, the iPOR and the GOR. It was found that the activities did not strictly depend on the Co content and that while different trends were observed for the different reactions, supposedly due to different requirements for the active sites, similarities were recorded in correlation with phase separation that the

material experiences upon Co incorporation. However, no correlation between activity trends and (electrochemical) surface area were observed. Analysis of GOR products by HPLC revealed that the metal and phase composition of the $\text{LaFe}_{1-x}\text{Co}_x\text{O}_3$ samples also have an influence on the relative concentrations of electrolysis products, demonstrating a trade-off between activity and selectivity.

Experimental Section

Materials and Reagents

Lanthanum(III) nitrate hexahydrate (99.9% La, abcr), iron(III) nitrate nonahydrate ($\geq 96\%$, Carl Roth), cobalt(II) nitrate hexahydrate ($\geq 98\%$, Carl Roth), sodium hydroxide (98.5%, Carl Roth), sodium carbonate ($\geq 99.5\%$, VWR International), ethanol (VWR Chemicals, abs.), Nafion (Sigma-Aldrich, 5 wt% in lower aliphatic alcohols and water), 2-propanol (VWR Chemicals, abs.), glycerol (Fisher Scientific, $\geq 99\%$), sulfuric acid (Merck, 98%), ammonium formate (Sigma-Aldrich, $\geq 99\%$), sodium D-lactate (Aldrich, 99%), glycolic acid (Sigma-Aldrich, 99%), calcium L(-)-glycerate dihydrate (Alfa Aesar), tartaric acid (Sigma-Aldrich, $\geq 97\%$), oxalic acid (Fluorochem), and acetic acid (Sigma-Aldrich, 99.8%) were used as purchased without further purification. KOH solutions (Fisher Scientific, 86.7%) were purified using a Chelex 100 cation-exchange resin (Sigma-Aldrich, 50–100 mesh) for removing metal impurities. All aqueous solutions used for electrochemical measurements were prepared using ultrapure water. Solutions for synthesis were prepared with deionised water.

Catalyst Synthesis

Synthesis of $\text{LaFe}_{1-x}\text{Co}_x\text{O}_3$ was conducted via automated coprecipitation at constant pH followed by thermal decomposition according to a procedure reported in detail elsewhere.^[52] In brief, an OptiMax 1001 (Mettler Toledo) synthesis workstation with a single-walled glass reactor inside a solid-state thermostat was used for the simultaneous computer-controlled dosing of metal salt solution (0.8 mol L^{-1} total ionic concentration with the general composition of $\text{La}^{3+}:\text{Fe}^{3+}:\text{Co}^{2+} = 1:(1-x):x$ where x was varied between 0 and 0.7) and precipitation agent (1.2 mol L^{-1} NaOH and 0.18 mol L^{-1} Na_2CO_3) at 10°C and constant pH 9.5 stirred at 300 rpm under N_2 flow. After a 60 min aging step at 10°C , the synthesis products were isolated by centrifugation at 6000 rpm for 2 min, washed with deionised water until the supernatant showed conductivities below 0.1 mS cm^{-1} during 2 consecutive runs, and dried at 80°C for 12 h. Finally, the as-prepared powders were calcined in stagnant air at 800°C for 3 h at a heating rate of 2°C min^{-1} in a muffle furnace (Nabertherm B150).

Materials Characterisation

The calcined samples were characterised by X-ray photoelectron spectroscopy (XPS) using an Ulvac-Phi VersaProbe II. N_2 adsorption-desorption measurements were conducted with the NOVA3000e (Quantachrome Instruments) at -196°C after degassing (80°C , 2 h in vacuum) and Brunauer-Emmett-Teller surface areas were calculated from p/p_0 data between 0.05 and 0.3. Powder X-ray diffraction (XRD) was conducted in the 2θ range between 5° and 90° using a Bruker D8 Advance setup with Bragg-Brentano geometry and position-sensitive LYNXEYE detector with Ni-filtered $\text{Cu-K}\alpha$ radiation (Bruker), 0.3 s counting time and a step size of

0.018. Rietveld refinement was performed with the TOPAS software (Bruker).

Electrocatalytic Activity

For the determination of the electrocatalytic activity a three-electrode setup was used consisting of a Pt mesh counter electrode, a $\text{Ag}|\text{AgCl}|\text{KCl}$ (3 M) reference electrode and a catalyst-modified glassy carbon rotating disk electrode (RDE) (0.1134 cm^2 geometric area) as the working electrode. The counter electrode was kept in a compartment separated by a glass frit during the measurements. Catalyst inks were prepared by dispersing 5 mg mL^{-1} catalyst in a mixture of water, ethanol and as-purchased Nafion solution (49:49:2 vol%) by sonicating for 15 min followed by tip sonication for 1 min (25% amplitude, 1 s on/1 s off). The glassy carbon electrode was polished with $0.05 \mu\text{m}$ alumina powder to mirror finish, rinsed, dried, and modified by drop-casting $4.8 \mu\text{L}$ of catalyst ink to achieve a total catalyst loading of $212 \mu\text{g cm}^{-2}$. The catalyst film was left to dry at ambient conditions under a glass beaker. As electrolytes, either 1 M KOH, or 1 M of the respective alcohol (2-propanol or glycerol) dissolved in 1 M KOH were used. The electrolyte was purged with Ar for at least 15 min and an Ar flow was upheld near the surface of the electrolyte during the measurements. The applied potentials were controlled with an Autolab PGSTAT302N potentiostat (Metrohm) and the NOVA 1.11 software. Electrochemical impedance spectroscopy (EIS) was conducted at open-circuit potential (OCP) in the frequency range between 100 kHz and 100 Hz using 10 mV (RMS) amplitude to determine the uncompensated resistance (R_u). Subsequently, cyclic voltammetry was conducted at 100 mV s^{-1} scan rate in the potential range between 0 and 0.4 V vs. $\text{Ag}|\text{AgCl}|\text{KCl}$ (3 M) until reproducible voltammograms were observed, followed by a linear sweep voltammogram (LSV) recorded with a scan rate of 5 mV s^{-1} and a rotation rate of 1600 rpm in the potential range between 0 and 0.8 V vs. $\text{Ag}|\text{AgCl}|\text{KCl}$ (3 M) for the oxygen evolution reaction (OER) and between 0 and 0.7 V vs. $\text{Ag}|\text{AgCl}|\text{KCl}$ (3 M) for the oxidation of isopropanol (iPOR) and of glycerol (GOR). All measurements were conducted in triplicate to ensure reproducibility (cf. Figure S13) and the average of the three individual measurements is reported in the main manuscript (Figure 2).

Determination of Double Layer Capacitance

The double layer capacitance C_{DL} was determined for the different catalysts according to a previously reported procedure.^[62] In short, cyclic voltammograms were recorded at different scan rates (0.1, 0.25, 0.5, 0.75 and 1 V s^{-1}) in a redox process-free potential window of 0.5 V centred at open circuit potential (OCP) until reproducible voltammograms were obtained. Currents from the anodic and cathodic scans were extracted and plotted against their respective scan rates. The resulting current vs scan rate plots were fitted using an allomeric regression to extract C_{DL} . The mean of the anodic and cathodic C_{DL} has been reported as the average C_{DL} .

Chronoamperometry in the Presence of Glycerol

Chronoamperometric measurements were conducted in a three-electrode circular flow-through electrolyser consisting of a Ni wire counter electrode, a double-junction $\text{Ag}|\text{AgCl}|\text{KCl}$ (3 M) reference electrode with the outer chamber filled with 1 M KOH, and a catalyst-modified carbon paper (H23C2, Freudenberg, 0.95 cm^2 geometric area exposed to the electrolyte) as the working electrode. Onto the carbon paper $98 \mu\text{L}$ of catalyst ink was drop-cast, which was prepared by dispersing 20 mg mL^{-1} catalyst in a mixture of ethanol and as-purchased Nafion solution (98:2 vol%)

by sonicating for 15 min and subsequent tip sonication for 1 min (25% amplitude, 1 s on/1 s off), achieving a total catalyst loading of approximately 1 mg cm^{-2} . The catalyst film was dried under ambient conditions. The working and counter electrodes were positioned in different compartments which were separated by an anion exchange membrane (Fumatech fumasep FAA-3-PK-130) which, prior to the measurement, was soaked in 1 M KOH. The anolyte reservoir was filled with 6 mL of 1 M glycerol in 1 M KOH while the catholyte reservoir contained 1 M KOH. An approximately 5.3 mL min^{-1} flow rate was applied using a peristaltic pump (Spetec Perimax). A VSP-300 potentiostat (BioLogic) controlled by the EC Lab software was used for the electrochemical measurements. Prior to chronoamperometry in the presence of glycerol, the following procedure was performed in 1 M KOH solution: (1) OCP was recorded for 1 min, (2) EIS measurements were conducted at OCP in the frequency range between 100 kHz and 100 Hz with an amplitude of 10 mV (RMS), and (3) 20 cyclic voltammograms were recorded between 0 and 0.4 V vs. Ag|AgCl|KCl (3 M) at a scan rate of 100 mVs^{-1} . Then, the electrolyte in the anode reservoir was exchanged to the KOH solution containing the glycerol (1 M). Subsequently, a LSV was recorded between 0 and 0.55 V vs. Ag|AgCl|KCl (3 M) and the end potential was held for 48 h. $350 \mu\text{L}$ samples of the anolyte were taken at different time intervals ($t=0, 24, \text{ and } 48 \text{ h}$) for product analysis.

Data Processing of the Electrochemical Measurements

All potentials (E_{recorded}) are reported with respect to the reversible hydrogen electrode (RHE) according to Equation (1) considering the formal potential of the reference electrode ($E_{0, \text{Ag}|\text{AgCl}|\text{KCl} (3 \text{ M})}$), namely 0.21 V, and the pH of the solution. The respective pH value was obtained taking into account the molar concentration of hydroxide in the electrolyte and using the literature value of 0.766 for the activity of water (γ) according to Equation (2).^[73] In addition to this, the ohmic-drop between the working and the reference electrodes was corrected by considering the uncompensated resistance R_u obtained from EIS measurements and the current measured (i).

$$E_{\text{RHE}} = E_{\text{recorded}} + E_{0, \text{Ag}|\text{AgCl}|\text{KCl} (3 \text{ M})} + 0.059 \cdot \text{pH} - R_u \cdot i \quad (1)$$

$$\text{pH} = 14 + \log [\text{OH}^-] + \log(\gamma) \quad (2)$$

Product Analysis

An electrolyte sample ($350 \mu\text{L}$) was collected at the start of electrolysis in the presence of glycerol, and after 24 and 48 h for product analysis by HPLC. To perform the measurements, the samples were acidified by adding $350 \mu\text{L}$ of 0.53 M sulfuric acid in order to quench possible follow-up reactions and, thus, avoid further transformation of intermediates via chemical reaction in solution.^[27] Subsequently, the acidified sample was filtered with a $0.2 \mu\text{m}$ syringe filter to protect the HPLC system from any residual particles. HPLC measurements were performed with the Dionex ICS-5000+ system (ThermoFisher) connected to a refractive index (RI) detector (Knauer RefractoMax520) and a diode array detector (UV/VIS, Dionex UltiMate 3000). Products were separated with an ion-exclusion column and precolumn (Bio-Rad Aminex HPX-87H) heated at 70°C using $4 \text{ mM H}_2\text{SO}_4$ as eluent at a flow rate of 0.6 mL min^{-1} . Product quantification was enabled by calibration using commercially available reference compounds in a concentration range of 0.1 mM to 10 mM extended to 1000 mM for glycerol and formic acid. As an example, chromatograms of the standard solutions, containing the respective compounds at 10 mM concentration are shown in Figure S15 for the RI detector. Most

products were detected satisfactorily by the RI detector, however, glycerol and formic acid overlap. Therefore, the UV/VIS detector was used for formic acid detection at 220 nm where glycerol is not UV-active. The glycerol conversion was determined by calculating the area that formic acid (FA) would have in the RI scale using the FA concentration measured at 220 nm and, subsequently, subtracting it from the glycerol area recorded with the RI detector, thus obtaining the glycerol concentration via the respective calibration factors. By using the anolyte volume corrected by the sampling volume taken up to this point in the course of the measurement this value was converted to moles and used as the initial number of moles of glycerol (n_{G_0}). Thus, Equation (3) was used where n_{G_i} denominates the moles of glycerol remaining in the electrolyte at different reaction times.

$$\text{Conversion (\%)} = (n_{\text{G}_0} - n_{\text{G}_i}) \cdot 100/n_{\text{G}_0} \quad (3)$$

Acknowledgements

Financial support is acknowledged by the Deutsche Forschungsgemeinschaft (DFG, German Research Foundation) in the framework of the research unit FOR 2982 "UNODE – Unusual Anode Reactions" (413163866) and the Collaborative Research Center/Transregio "Heterogeneous Oxidation Catalysis in the Liquid Phase" -388390466-TRR 247 (Project C1, A2, and S). MB acknowledges financial support from the Mercator Research Center Ruhr (MERCUR, Pe-2018-0034). Open Access funding enabled and organized by Projekt DEAL.

Conflict of Interest

The authors declare no conflict of interest.

Data Availability Statement

The data that support the findings of this study are available from the corresponding author upon reasonable request.

Keywords: oxygen evolution reaction · glycerol oxidation · isopropanol oxidation · electrocatalytic activity · perovskites

- [1] M. Yu, E. Budiyo, H. Tüysüz, *Angew. Chem. Int. Ed.* **2022**, *61*, e202103824, *Angew. Chem.* **2022**, *134*, e202103824.
- [2] S. Wang, A. Lu, C.-J. Zhong, *Nano Convergence* **2021**, *8*, 4.
- [3] B. Garlyyev, S. Xue, J. Fichtner, A. S. Bandarenka, C. Andronescu, *ChemSusChem* **2020**, *13*, 2513.
- [4] H. Lin, G.-L. Chen, Z.-S. Zheng, J.-Z. Zhou, S.-P. Chen, Z.-H. Lin, *Acta Phys.-Chim. Sin.* **2005**, *21*, 1280 DOI: 10.3866/PKU.WHXB20051117.
- [5] C. Dai, L. Sun, H. Liao, B. Khezri, R. D. Webster, A. C. Fisher, Z. J. Xu, *J. Catal.* **2017**, *356*, 14.
- [6] C. H. Lam, A. J. Bloomfield, P. T. Anastas, *Green Chem.* **2017**, *19*, 1958.
- [7] N. Razali, A. Z. Abdullah, *Appl. Catal. A* **2017**, *543*, 234.
- [8] S. Bagheri, N. M. Julkapli, W. A. Yehye, *Renewable Sustainable Energy Rev.* **2015**, *41*, 113.
- [9] G. Dodekatos, S. Schünemann, H. Tüysüz, *ACS Catal.* **2018**, *8*, 6301.
- [10] Q. Shi, C. Zhu, D. Du, Y. Lin, *Chem. Soc. Rev.* **2019**, *48*, 3181.
- [11] T. Reier, H. N. Nong, D. Teschner, R. Schlögl, P. Strasser, *Adv. Energy Mater.* **2017**, *7*, 1601275.
- [12] E. S. Y. Matsumoto, *Mater. Chem. Phys.* **1986**, *14*, 397.
- [13] H. Habibi, E. Dadashpour, *Electrochim. Acta* **2013**, *88*, 157.

- [14] C. Jin, X. Sun, Z. Chen, *Chem. Eng. Technol.* **2012**, *35*, 1064.
- [15] H. Liao, Z. Qiu, Q. Wan, Z. Wang, Y. Liu, N. Yang, *ACS Appl. Mater. Interfaces* **2014**, *6*, 18055.
- [16] I. d. A. Rodrigues, J. P. I. de Souza, E. Pastor, F. C. Nart, *Langmuir* **1997**, *13*, 6829.
- [17] K. M. Waldie, K. R. Flajlslik, E. McLoughlin, C. E. D. Chidsey, R. M. Waymouth, *J. Am. Chem. Soc.* **2017**, *139*, 738.
- [18] J. Ye, J. Liu, C. Xu, S. Jiang, Y. Tong, *Electrochem. Commun.* **2007**, *9*, 2760.
- [19] W. Zhou, C. Wang, J. Xu, Y. Du, P. Yang, *Mater. Chem. Phys.* **2010**, *123*, 390.
- [20] P. Khanipour, F. D. Speck, I. Mangoufis-Giasin, K. J. J. Mayrhofer, S. Cherevko, I. Katsounaros, *ACS Appl. Mater. Interfaces* **2020**, *12*, 33670.
- [21] L. Fan, B. Liu, X. Liu, N. Senthilkumar, G. Wang, Z. Wen, *Energy Technol.* **2021**, *9*, 2000804.
- [22] Y. Zhou, Y. Shen, J. Piao, *ChemElectroChem* **2018**, *5*, 1636.
- [23] N. Woz, A. Brandner, P. Claus, *J. Phys. Chem. C* **2010**, *114*, 1164.
- [24] H. Wang, L. Thia, N. Li, X. Ge, Z. Liu, X. Wang, *Appl. Catal. B* **2015**, *166–167*, 25.
- [25] J. Qi, L. Xin, D. J. Chadderdon, Y. Qiu, Y. Jiang, N. Benipal, C. Liang, W. Li, *Appl. Catal. B* **2014**, *154–155*, 360.
- [26] C. A. Ottoni, S. G. Da Silva, R. F. B. de Souza, A. O. Neto, *Ionics* **2016**, *22*, 1167.
- [27] Y. Kwon, K. J. P. Schouten, M. T. M. Koper, *ChemCatChem* **2011**, *3*, 1176.
- [28] Y. Kwon, Y. Birdja, I. Spanos, P. Rodriguez, M. T. M. Koper, *ACS Catal.* **2012**, *2*, 759.
- [29] S. Kongjao, S. Damronglerd, M. Hunsom, *J. Appl. Electrochem.* **2011**, *41*, 215.
- [30] D. Hiltrop, S. Cychy, K. Elumeeva, W. Schuhmann, M. Muhler, *Beilstein J. Org. Chem.* **2018**, *14*, 1428.
- [31] A. C. Garcia, Y. Y. Birdja, G. Tremiliosi-Filho, M. T. Koper, *J. Catal.* **2017**, *346*, 117.
- [32] M. S. Ahmad, C. K. Cheng, R. Kumar, S. Singh, K. A. Saeed, H. R. Ong, H. Abdullah, M. R. Khan, *Electroanalysis* **2020**, *32*, 1139.
- [33] P. J. Kulesza, I. S. Pieta, I. A. Rutkowska, A. Wadas, D. Marks, K. Klak, L. Stobinski, J. A. Cox, *Electrochim. Acta* **2013**, *110*, 474.
- [34] H. A. Gasteiger, N. M. Markovic, P. N. Ross, Jr., *J. Phys. Chem.* **1995**, *99*, 8290.
- [35] A. Ashok, A. Kumar, J. Ponraj, S. A. Mansour, F. Tarlochan, *J. Electrochem. Soc.* **2018**, *165*, J3301–J3309.
- [36] L. L. Carvalho, F. Colmati, A. A. Tanaka, *Int. J. Hydrogen Energy* **2017**, *42*, 16118.
- [37] M. Fleischmann, K. Korinek, D. Pletcher, *J. Electroanal. Chem. Interfacial Electrochem.* **1971**, *31*, 39.
- [38] B. Habibi, N. Delnavaz, *RSC Adv.* **2016**, *6*, 31797.
- [39] J. Han, Y. Kim, H. W. Kim, D. H. Jackson, D. Lee, H. Chang, H.-J. Chae, K.-Y. Lee, H. J. Kim, *Electrochem. Commun.* **2017**, *83*, 46.
- [40] M. S. Houache, E. Cossar, S. Ntais, E. A. Baranova, *J. Power Sources* **2018**, *375*, 310.
- [41] V. L. Oliveira, C. Morais, K. Servat, T. W. Napporn, G. Tremiliosi-Filho, K. B. Kokoh, *J. Electroanal. Chem.* **2013**, *703*, 56.
- [42] Q. Shao, J. Song, Y. Feng, X. Zhu, X. Huang, *ChemCatChem* **2018**, *10*, 3647.
- [43] D. E. Simpson, K. E. Juda, D. Roy, *Electrocatalysis* **2018**, *9*, 86.
- [44] X. Han, H. Sheng, C. Yu, T. W. Walker, G. W. Huber, J. Qiu, S. Jin, *ACS Catal.* **2020**, *10*, 6741.
- [45] M. S. E. Houache, K. Hughes, R. Safari, G. A. Botton, E. A. Baranova, *ACS Appl. Mater. Interfaces* **2020**, *12*, 15095.
- [46] Y. Li, X. Wei, L. Chen, J. Shi, M. He, *Nat. Commun.* **2019**, *10*, 5335.
- [47] C. Liu, M. Hirohara, T. Maekawa, R. Chang, T. Hayashi, C.-Y. Chiang, *Appl. Catal. B* **2020**, *265*, 118543.
- [48] V. L. Oliveira, C. Morais, K. Servat, T. W. Napporn, G. Tremiliosi-Filho, K. B. Kokoh, *Electrochim. Acta* **2014**, *117*, 255.
- [49] A. C. Brix, D. M. Morales, M. Braun, D. Jambrec, J. R. C. Junqueira, S. Cychy, S. Seisel, J. Masa, M. Muhler, C. Andronescu, W. Schuhmann, *ChemElectroChem* **2021**, *8*, 2336.
- [50] P. V. Santiago, C. C. Lima, J. L. Bott-Neto, P. S. Fernández, C. A. Angelucci, J. Souza-Garcia, *J. Electroanal. Chem.* **2021**, *896*, 115198.
- [51] D. Antipin, M. Risch, *J. Phys. Energy* **2020**, *2*, 032003, DOI: 10.1088/2515-7655/ab812f.
- [52] M. Dreyer, M. Krebs, S. Najafshirvari, A. Rabe, K. Friedel Ortega, M. Behrens, *Catalysts* **2021**, *11*, 550.
- [53] Y. Guo, Y. Tong, P. Chen, K. Xu, J. Zhao, Y. Lin, W. Chu, Z. Peng, C. Wu, Y. Xie, *Adv. Mater.* **2015**, *27*, 5989.
- [54] W. T. Hong, M. Risch, K. A. Stoerzinger, A. Grimaud, J. Suntivich, Y. Shao-Horn, *Energy Environ. Sci.* **2015**, *8*, 1404.
- [55] J. O'M. Bockris, T. Otagawa, *J. Electrochem. Soc.* **1984**, *131*, 290.
- [56] R. A. Rincón, E. Ventosa, F. Tietz, J. Masa, S. Seisel, V. Kuznetsov, W. Schuhmann, *ChemPhysChem* **2014**, *15*, 2810.
- [57] P. P. Lopes, D. Y. Chung, X. Rui, H. Zheng, H. He, P. Farinazzo Bergamo Dias Martins, D. Strmcnik, V. R. Stamenkovic, P. Zapol, J. F. Mitchell, R. F. Klie, N. M. Markovic, *J. Am. Chem. Soc.* **2021**, *143*, 2741.
- [58] Y. Sun, R. Li, X. Chen, J. Wu, Y. Xie, X. Wang, K. Ma, L. Wang, Z. Zhang, Q. Liao, Z. Kang, Y. Zhang, *Adv. Energy Mater.* **2021**, *11*, 2003755.
- [59] A. Füngelings, A. Koul, M. Dreyer, A. Rabe, D. M. Morales, W. Schuhmann, M. Behrens, R. Pentcheva, *Chem. Eur. J.* **2021**, *27*, 17145.
- [60] B. Alkan, S. Cychy, S. Varhade, M. Muhler, C. Schulz, W. Schuhmann, H. Wiggers, C. Andronescu, *ChemElectroChem* **2019**, *6*, 4266.
- [61] M. Dreyer, D. Cruz, U. Hagemann, P. Zeller, M. Heidelmann, S. Salamon, J. Landers, A. Rabe, K. F. Ortega, S. Najafshirvari, H. Wende, N. Hartmann, A. Knop-Gericke, R. Schlögl, M. Behrens, *Chem. Eur. J.* **2021**, *27*, 17127.
- [62] D. M. Morales, M. Risch, *J. Phys. Energy* **2021**, *3*, 034013, DOI: 10.1088/2515-7655/abee33.
- [63] Y. Wu, C. Cordier, E. Berrier, N. Nuns, C. Dujardin, P. Granger, *Appl. Catal. B* **2013**, *140–141*, 151.
- [64] N. A. Merino, B. P. Barbero, P. Ruiz, L. E. Cadús, *J. Catal.* **2006**, *240*, 245.
- [65] Y. Duan, S. Sun, S. Xi, X. Ren, Y. Zhou, G. Zhang, H. Yang, Y. Du, Z. J. Xu, *Chem. Mater.* **2017**, *29*, 10534.
- [66] D. A. Corrigan, *J. Electrochem. Soc.* **1987**, *134*, 377.
- [67] L. Trotochaud, S. L. Young, J. K. Ranney, S. W. Boettcher, *J. Am. Chem. Soc.* **2014**, *136*, 6744.
- [68] S. Anantharaj, S. Kundu, S. Noda, *Nano Energy* **2021**, *80*, 105514.
- [69] S. Aleksovskaja, S. Dimitrovska-Lazova, V. Mirceski, *Studia* **2015**, *LX*, 53.
- [70] I. G. Casella, T. R. I. Cataldi, A. M. Salvi, E. Desimoni, *Anal. Chem.* **1993**, *65*, 3143.
- [71] M.-S. Ekrami-Kakhki, Z. Yavari, J. Saffari, S. A. Ekrami-Kakhki, *J. Electron. Eng.* **2016**, *4*, 88.
- [72] J. Masa, C. Andronescu, W. Schuhmann, *Angew. Chem. Int. Ed.* **2020**, *59*, 15298.
- [73] L. A. Bromley, *AIChE J.* **1973**, *19*, 313.

Manuscript received: January 24, 2022

Accepted manuscript online: January 24, 2022